

Dynamic structural disorder in supported nanoscale catalysts

J. J. Rehr and F. D. Vila

Citation: *The Journal of Chemical Physics* **140**, 134701 (2014); doi: 10.1063/1.4869178

View online: <http://dx.doi.org/10.1063/1.4869178>

View Table of Contents: <http://scitation.aip.org/content/aip/journal/jcp/140/13?ver=pdfcov>

Published by the [AIP Publishing](#)

Articles you may be interested in

[Active sites of ligand-protected Au₂₅ nanoparticle catalysts for CO₂ electroreduction to CO](#)

J. Chem. Phys. **144**, 184705 (2016); 10.1063/1.4948792

[DFT-D2 simulations of water adsorption and dissociation on the low-index surfaces of mackinawite \(FeS\)](#)

J. Chem. Phys. **144**, 174704 (2016); 10.1063/1.4947588

[A classical trajectory study of the intramolecular dynamics, isomerization, and unimolecular dissociation of HO₂](#)

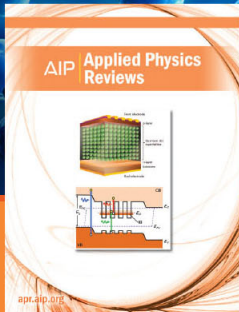
J. Chem. Phys. **139**, 084319 (2013); 10.1063/1.4818879

[Charge redistribution in core-shell nanoparticles to promote oxygen reduction](#)

J. Chem. Phys. **130**, 194504 (2009); 10.1063/1.3134684

[Influence of initial oxygen coverage and magnetic moment on the NO decomposition on rhodium \(111\)](#)

J. Chem. Phys. **122**, 154702 (2005); 10.1063/1.1878692



NEW Special Topic Sections

NOW ONLINE
Lithium Niobate Properties and Applications:
Reviews of Emerging Trends

AIP | Applied Physics
Reviews

Dynamic structural disorder in supported nanoscale catalysts

J. J. Rehr and F. D. Vila

Department of Physics, University of Washington, Seattle, Washington 98195, USA

(Received 9 September 2013; accepted 4 March 2014; published online 1 April 2014)

We investigate the origin and physical effects of “dynamic structural disorder” (DSD) in supported nano-scale catalysts. DSD refers to the intrinsic fluctuating, inhomogeneous structure of such nano-scale systems. In contrast to bulk materials, nano-scale systems exhibit substantial fluctuations in structure, charge, temperature, and other quantities, as well as large surface effects. The DSD is driven largely by the stochastic librational motion of the center of mass and fluxional bonding at the nanoparticle surface due to thermal coupling with the substrate. Our approach for calculating and understanding DSD is based on a combination of real-time density functional theory/molecular dynamics simulations, transient coupled-oscillator models, and statistical mechanics. This approach treats thermal and dynamic effects over multiple time-scales, and includes bond-stretching and -bending vibrations, and transient tethering to the substrate at longer ps time-scales. Potential effects on the catalytic properties of these clusters are briefly explored. Model calculations of molecule-cluster interactions and molecular dissociation reaction paths are presented in which the reactant molecules are adsorbed on the surface of dynamically sampled clusters. This model suggests that DSD can affect both the prefactors and distribution of energy barriers in reaction rates, and thus can significantly affect catalytic activity at the nano-scale. © 2014 AIP Publishing LLC. [<http://dx.doi.org/10.1063/1.4869178>]

I. INTRODUCTION

The structure and behavior of materials at the nanoscale are both of fundamental and technological importance. They are particularly relevant to the understanding of supported nanoscale catalysts. This challenging problem is complicated by the fact that nano-scale properties differ from those of bulk condensed systems, especially at high temperatures. Their unusual thermodynamic properties have been widely recognized at structural,¹ spectroscopic,² and catalytic³ levels. These properties differ from the bulk since the thermodynamic limit does not apply for small N , where N refers to the number of atoms in the nanocluster. For example, cluster surface effects of $O(N^{2/3})$ in extensive physical quantities (i.e., quantities proportional to N like total cluster energy) are crucial, and thus nano-scale systems are necessarily inhomogeneous. In addition supported nano-scale catalysts exhibit an intrinsic fluctuating, inhomogeneous structure, referred to here as dynamic structural disorder (DSD).⁴ Moreover, statistical physics arguments imply that nano-scale systems exhibit substantial $O(1/\sqrt{N})$ fluctuations in local temperature. Thus, in contrast to bulk solids, these systems have no well-defined static “mechanical equilibrium structure,” particularly at high temperatures. The presence of these intrinsic fluctuations suggest that it is useful to examine their behavior from a dynamical perspective. This approach is in contrast to conventional surface science methodology typically based on static structural properties. Indeed, there has been a growing interest in such real-time approaches in recent years.⁴⁻⁷ The possible implications of DSD on catalytic properties at the nanoscale are also briefly explored. Dynamic effects have been postulated to play a role in other treatments of catalysis, ranging from het-

erogeneous catalysis^{8,9} at surfaces and in the catalytic activity in biostructures.^{10,11} The difference in the treatment here is the emphasis on the effects of nano-scale dynamics on catalytic properties, which are investigated using nudged-elastic-band (NEB) transition state theory (TST) calculations.

Our approach for modelling the effects of DSD is based on a concept dubbed picturesquely as “Shake-Rattle-and-Roll” (SRR). This approach was inspired by observations of unusual behavior in nanoscale supported Pt and Pt-alloy catalysts: For example, x-ray absorption spectra (XAS) studies showed that small Pt nano-clusters exhibit negative thermal expansion, anomalously large disorder, and temperature dependent shifts in XAS threshold energies.⁵ These anomalous properties were subsequently explained by finite-temperature density functional theory/molecular dynamics (DFT/MD) calculations, which showed that they are dynamical in origin, involving multiple time-scales.⁶ They include (1) fast bond vibrations (i.e., *shaking*), (2) soft anharmonic or fluxional modes, particularly involving the nano-particle surface atoms; and (3) librational motion of the center of mass (CM), which is due to the thermal contact of the nano-clusters tethered to the support bonding sites. As discussed below, these CM dynamics are analogous to hindered 2-dimensional Brownian motion.⁶ These longer-time whole-cluster dynamics have been previously shown to be important in the characterization of epitaxial nanoclusters.¹²⁻¹⁵ When combined with the stochastic thermal coupling to the support, these low-frequency modes induce a *rattle*-like motion in the system, typically at sub-THz frequencies. At longer time scales (tens of ps for supported Pt clusters on γ -alumina at high temperatures), bonding to the support is transient. When those bonds break, the nano-clusters can then *roll* or slide to new

positions on the support. This behavior differs from that in previous studies of diffusion,^{12–15} in that the characteristic time-scale is set by the librational motion of the cluster with respect to the support, rather than the frequency of individual atomistic events. According to the crystallite model of sintering, the combined motion of many such clusters typically leads to reduced catalytic activity.¹⁶ The rattle-like motion has been recently⁴ interpreted as dynamic structural disorder, in contrast to static bond distortions or substitutional disorder typical in condensed systems. Instead, the DSD is “non-equilibrium” in character, in the sense that the system exhibits fluctuations from mechanical and thermal equilibrium, even though, of course, the full system (cluster plus support) is in overall “thermal-equilibrium,” with a well defined global temperature T . Thus the mean geometric structure of nano-clusters is amorphous and fluctuating, rather like that in a partly-melted solid. Indeed, DSD affects the nano-cluster behavior through stochastic fluctuations in structure, cluster charge, thermal fluctuations, and center of mass position.

These remarkable observations have motivated us to reinvestigate the structure and catalytic behavior of supported nanoscale catalysts in terms of their dynamic behavior. To this end, we investigate the SRR concept based on a combination of real-time DFT/MD simulations, transient coupled-oscillator models, and statistical mechanics. Given the computational demands of DFT/MD simulations, we focus primarily on the few ps DSD regime. This regime is sufficient to capture the “shake” and “rattle” dynamics, and the faster components of the “roll” dynamics. However, the nanosecond dynamics involved in longer-range nanoparticle drift over the support are taken into account statistically, by sampling results for a number of independent trajectories.

As discussed below, the SRR model can explain the anomalous properties observed for supported nano-clusters, including both DSD and charge fluctuations. As an illustration we have applied this approach to calculations of both the interaction between the supported nanocatalysts and prototypical molecules, and their dissociation reaction paths. These show that the DSD provides a mechanism for increasing reaction rates. Although still rather preliminary, the SRR model offers tantalizing insights into dynamic mechanisms that contribute to catalytic processes.

II. DYNAMIC STRUCTURAL DISORDER

A. Structure and disorder in nanoclusters

In order to investigate DSD within the framework of SRR, and to differentiate DSD from other types of disorder, we consider the effect of large fluctuations on the dynamic structure and disorder of the cluster. This structure can be described formally as a point in $6N$ -dimensional phase space defining the nuclear coordinates and momenta $\{\vec{R}_i(t), \vec{P}_i(t), i = 1 \dots N\}$. Due to the fluctuations in the structure, e.g., the change in shape due to the librational motion and fluxional surface bonds, the cluster potential energy surface $V[\{\vec{R}_i\}, t]$ will also fluctuate on a time-scale comparable to the librational motion, which is much slower than typical bond vibrations. During that time the motion of the cluster is

vibrational with respect to the instantaneous minima on its PES, i.e., fluctuating equilibrium positions, denoted by \vec{R}_i . The fluctuating structure of the clusters can be characterized in terms of the pair-distribution function (PDF) $g(R)$, which is defined as the average distance between all bond pairs (i, j) in the cluster,

$$g(R) = \frac{1}{N(N-1)} \sum_{i \neq j} \langle \delta(R - |\vec{R}_i(t) - \vec{R}_j(t)|) \rangle. \quad (1)$$

This PDF can be measured in experiment. For example, the XAFS signal

$$\chi(k) = \int dR g(R) \frac{f_{\text{eff}}(k)}{kR^2} \sin(2kR + \Phi) e^{-2R/\lambda} \quad (2)$$

is closely related to the Fourier transform of $g(R)$. In conventional XAFS analysis, however, one usually restricts consideration to the near neighbor bonds, e.g., by Fourier filtering over the first coordination shell, which is described by the near-neighbor distribution function $\tilde{g}(R)$. Physical quantities of interest are then obtained from the cumulant moments of $\tilde{g}(R)$, e.g., the mean near-neighbor distance $\bar{R} = \langle R \rangle = \int dR R \tilde{g}(R)$, and the mean-square radial disorder (MSRD) by $\sigma^2 = \langle (R - \bar{R})^2 \rangle$.

We emphasize that the quantities \bar{R} and σ^2 refer to averages over the entire cluster and thus can give a misleading picture of the structure of inhomogeneous systems. This difference is important in the Pt nano-clusters, for which the mean Pt-Pt bond lengths and fluctuations depend on the local environment, and thus their locations inside the cluster. Simulations of σ^2 can be carried out in terms of the distribution of (partial) PDFs at each site $g(R) = \sum_i g_i(R)$. The local near-neighbor distributions $\tilde{g}_i(R)$ have net weights $\tilde{g}_i = \int dR \tilde{g}_i(R)$, mean near neighbor bond lengths $\bar{R}_i = \int dR R \tilde{g}_i(R)$, with fluctuations $\sigma_i^2 = \int dR (R - \bar{R}_i)^2 \tilde{g}_i(R)$. Consequently, the global average near-neighbor bond distance \bar{R} and MSRD σ^2 corresponding to experimental measurements are

$$\bar{R} = \sum_i \bar{R}_i \tilde{g}_i, \quad \sigma^2 = \bar{\sigma}_D^2 + \bar{\sigma}_V^2, \quad (3)$$

where the local bond vibrations (V) are $\bar{\sigma}_V^2 = \sigma_i^2 \tilde{g}_i$, and the mean-squared disorder (D) due to cluster inhomogeneity is $\bar{\sigma}_D^2 = \sum_i (\bar{R}_i - \bar{R})^2 \tilde{g}_i$. Interestingly, both of these contributions have DSD contributions from low frequency fluctuations.

B. DFT/MD calculations

In order to understand the fluctuations in structure quantitatively we have performed VASP²⁰ *ab initio* DFT/MD simulations of nanoscale Pt₁₀Sn₁₀ and Pt₁₅Sn₅ alloy clusters on γ -Al₂O₃ at 298 K and 598 K. All simulations were performed at the Γ point, using the PBE functional and a plane wave cutoff of 396 eV. Initial structures for the clusters were obtained by randomly substituting Sn atoms into the optimal gas phase Pt₂₀ cluster, and then placing them onto the “d” layer of the dehydroxylated [110] surface of γ -Al₂O₃. This surface is represented by 4 layers (2 fully relaxed and 2 frozen) in a supercell of 19.4 Å × 13.7 Å with an effective vacuum

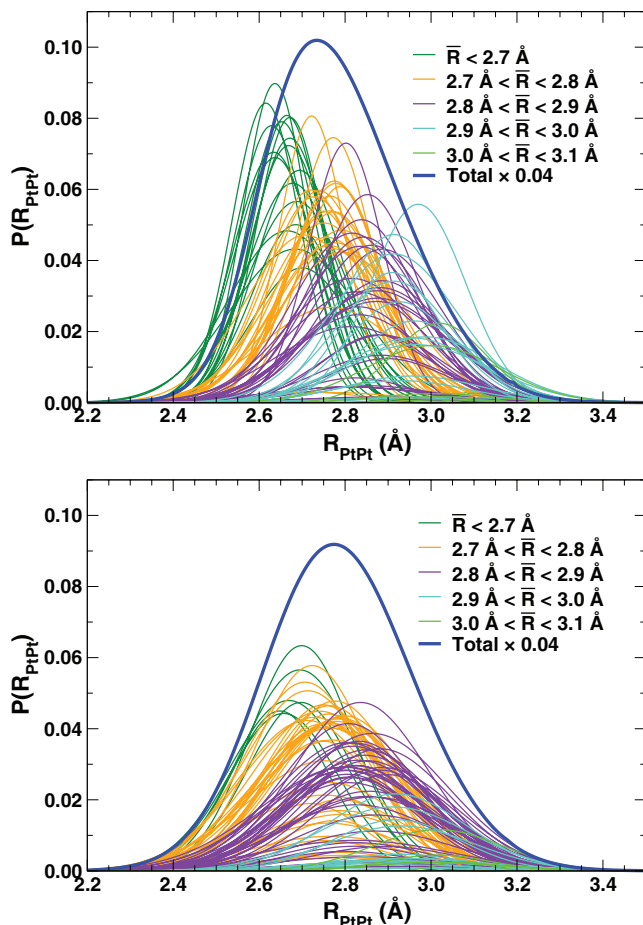


FIG. 1. Decomposition of the total pair distribution function of $\text{Pt}_{15}\text{Sn}_5$ on $\gamma\text{-Al}_2\text{O}_3$ at 298 K (top) and 598 K (bottom) into individual pair components. The different colors label the mean distance for the pair and the height of the distributions indicate their relative weight. Much of the width and asymmetry of the total near-neighbor distribution arises from cluster inhomogeneity.

separation of 16 Å. Four clusters were then relaxed to their optimal ground state conformations which were subsequently used to start the 298 K simulations. The initial structures for the 598 K runs were obtained by randomly sampling and quenching four conformations from the 298 K trajectories. All simulations used a 3 fs time step, which is adequate to capture the “fast” bond vibrations of the system. After an initial 3 ps thermalization period, statistical averages were acquired for 8 ps. These simulations provide a wealth of information on the electronic and structural properties of these systems, which have been described in detailed in Refs. 4 and 6. Briefly, we find that the particles are approximately hemi-spherical. Their volume increases with temperature for low Pt concentration while it decreases at high concentrations, in agreement with experimental observations⁵ of negative thermal expansion in pure Pt clusters. Analysis of the short-range order parameter indicates that the Sn atoms preferentially segregate to the particle surface, likely due to their markedly positive net charge. Pt atoms, which are mostly neutral, tend to form the core of the clusters. Finally, the effective contact between the Pt atoms and the support decreases with increasing Sn concentration.

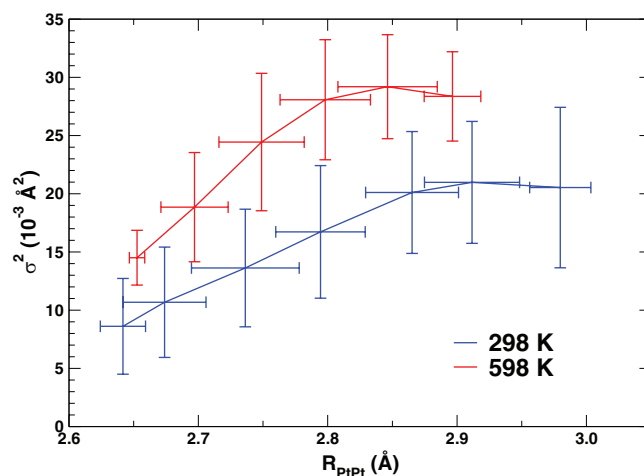


FIG. 2. Correlation between the mean Pt-Pt bond distances and their associated mean MSRDS for $\text{Pt}_{10}\text{Sn}_{10}$ on $\gamma\text{-Al}_2\text{O}_3$ at 298 K and 598 K. Both temperatures show similar behavior with weaker/longer bonds associated with larger MSRDS.

The decomposition of the $g(R)$ obtained from these MD simulations is shown in Fig. 1 vs. mean bond length. In particular, much of the width of the first neighbor peak in $g(R)$ comes from cluster inhomogeneity, and thus explains the anomalously large disorder observed for the nanoclusters.⁵ Moreover, the individual PDFs in Fig. 1 are not randomly distributed, suggesting a correlation between the mean Pt-Pt bond length and the associated MSRDS of the bond. This correlation is clearly shown in Fig. 2, with an increase in the MSRDS as the Pt-Pt bonds get longer/weaker. Another example of structural correlations is shown in Fig. 3, which depicts the mean Pt-Pt bond distance R_{PtPt} as a function of its distance to the center of the nanoparticle (R_{CC}). Bonds near the surface of the cluster ($R_{\text{CC}} \gtrsim 2.5$ Å) are shorter, as expected from their reduced number of near neighbors. This threshold is in good agreement with previous results⁴ showing that the interior-surface transition zone occurs between about 2.5 and 3 Å.

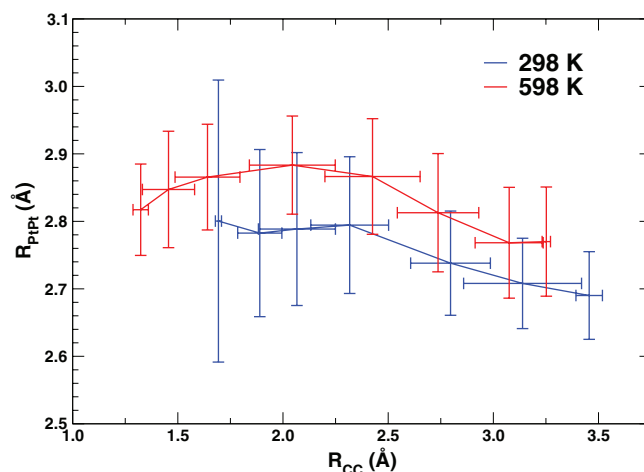


FIG. 3. Correlation between the Pt-Pt mean bond distances and their distance to the center of the nanoparticle (R_{CC}) for $\text{Pt}_{10}\text{Sn}_{10}$ on $\gamma\text{-Al}_2\text{O}_3$ at 298 K and 598 K. Both temperatures show similar behavior with shorter bonds near the surface of the particle.

C. Transient coupled oscillator model

While the DFT/MD simulations provide a quantitative account of DSD, they do not explicitly expose the underlying physical mechanisms that drive the dynamical disorder or explain the thermal behavior of tethered Pt nano-clusters. In order to understand their thermodynamic behavior within the SRR picture, we introduce a “transient coupled oscillator model.” That is, we consider the internal vibrations with respect to fluctuating instantaneous-equilibrium structures. This model is presumably valid over a ps time-scale which is long compared to typical bond vibrational periods. The dominant modes of the system coupled to the support thus consist of: (i) vibrational modes; (ii) soft and fluxional modes, particularly close to the cluster surface; and (iii) CM librational modes, i.e., soft modes about which the cluster center of mass fluctuates. For Pt, the vibrational modes are of THz scale, while the soft and librational modes are sub-THz. The model is transient, since anharmonicity and bond-breaking can be substantial, and hence the characteristic modes of oscillation fluctuate. The thermodynamic quantities of interest here can be obtained from the free energy, e.g., $\langle F(T) \rangle$ averaged over several such models, each of which can be calculated over sufficiently short (e.g., ps time-scale) time-intervals within a quasi-harmonic approximation using the relation,¹⁹

$$F(T) = E_0(\bar{R}) + kT \int d\omega \rho(\omega) \ln[2 \sinh(\beta\hbar\omega/2)]. \quad (4)$$

Here $\rho(\omega)$ is the total density of modes per unit frequency and $E_0(\bar{R})$ is the internal energy at the transient mean atomic positions. The thermodynamic average $\langle F(T) \rangle$ is given by the same expression but with $E_0(\bar{R})$ replaced by $\langle E_0(\bar{R}) \rangle$ and $\rho(\omega)$ by $\langle \rho(\omega) \rangle$. This approach is efficient, since despite the fluctuations in structure, the average spectrum $\langle \rho(\omega) \rangle$ is relatively stable and well defined. The term $E_0(\bar{R})$ is important since it contains the transient effects of charge fluctuations and affects changes in potential energy that dominate the reaction paths. The support provides both a heat bath and charge reservoir at fixed T which give rise to stochastic CM motion and DSD. Since we are primarily interested in catalytic behavior at high-temperatures, e.g., 300–600 °C, we focus our discussion here to the classical limit with mean phonon occupations $n(T) \approx kT/\hbar\omega \gg 1$. At 600 K this limit is a reasonable approximation for Pt, which has a Debye-temperature of 240 K and an equivalent Debye frequency of 5.2 THz. In this classical limit

$$F(T) = E_0(\bar{R}) + kT \int d\omega \rho(\omega) \ln(\beta\hbar\omega). \quad (5)$$

This statistical approach can also be directly compared to experiment, since observed physical properties are usually defined as averages over a statistical ensemble, and are equivalent to time-averages over a long time interval sufficient to cover the accessible phase space. Low frequency modes are important since $n(T)$ varies inversely with ω . However, the effect of breathing modes is expected to be small since for a 3-d bulk system $\rho(\omega) \approx \omega^2$ at long-wavelengths. From the identity $\bar{E} = \partial\beta F/\partial\beta$, we obtain a mean energy $\bar{E} = 3NkT$ at high temperatures, consistent with the equipar-

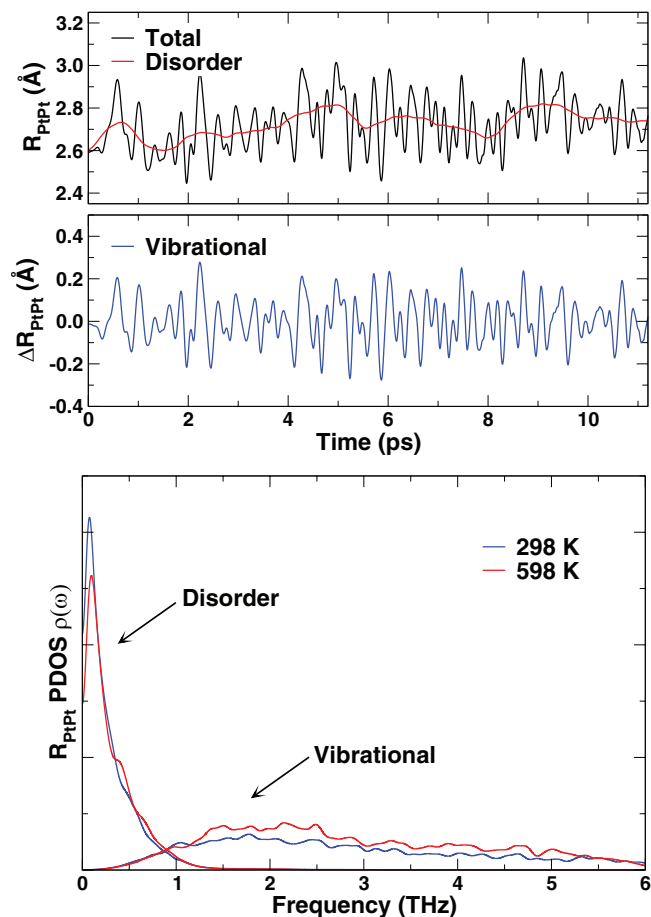


FIG. 4. (Top) Typical trajectory for a bound Pt-Pt pair in Pt₁₅Sn₅ on γ -Al₂O₃ at 298 K (black) decomposed into DSD (red) and vibrational (blue) components by applying a 0.5 THz low-pass filter. (Bottom) Average projected density of states for the vibrational and dynamic structural disorder components of bound Pt-Pt pairs in Pt₁₅Sn₅ as a function of temperature.

tion theorem. This energy includes contributions from the 2-d librational motion in the $x - y$ plane, which can be approximated by low frequency (sub THz) vibrational modes of the CM (Fig. 4). Thus the mean stochastic librational kinetic energy $(1/2)Mv_{lib}^2 = kT$. This result is the analog of Brownian motion, the difference being that such motion is hindered and 2-dimensional in character in nanoparticles tethered to the support. This stochastic CM motion is crucial to the origin of DSD and drives non-equilibrium fluctuations in the internal structure.

The low frequency DSD modes in Eq. (3) are particularly important, since they give large contributions to the MSRD

$$\sigma^2 = \frac{\hbar}{2\mu} \int d\omega \frac{\rho(\omega)}{\omega} \coth(\beta\hbar\omega/2) \approx \frac{kT}{\mu} \int d\omega \frac{\rho(\omega)}{\omega^2}, \quad (6)$$

where the expression on the right is the high temperature limit. Here μ refers to the reduced mass of a given bond pair, e.g., $M_{\text{Pt}}/2$ for Pt-Pt bonds. Thus it should be possible to distinguish DSD from conventional vibrations by filtering the density of modes $\rho(\omega)$. The result is shown in Fig. 4. Similarly, the contribution from each site σ_i^2 can be obtained by replacing $\rho(\omega)$ with the projected density of vibrational modes $\rho_i(\omega)$. In this way, one can analyze the net MSRD into

contributions from different positions in the cluster and their vibrational and DSD components. A similar expression can be used to calculate the librational fluctuations of the CM, with the reduced mass μ replaced by M_{CM} and ρ by the projected density of librational modes. Note that this expression implies that σ^2 for the Pt-Pt bonds is linear in T at high temperatures, with a slope depending on the inverse second moment of $\rho(\omega)$. Estimates of $\rho(\omega)$ can be obtained in various ways. For example, one approach is to use DFT/MD calculations of $\langle\sigma^2\rangle$, in real time over a sufficiently long interval τ ,

$$\langle\sigma^2\rangle = \frac{1}{\tau} \int_0^\tau dt \sigma^2(t) = \int d\omega \sigma^2(\omega), \quad (7)$$

where $\sigma^2(\omega) = \rho(\omega)/\mu\omega^2$. Such real-time calculations naturally account for the transient coupled-oscillator motion and effects of charge fluctuations on the dynamics of the cluster, as illustrated in Fig. 4 (bottom). Detailed information on the various times time-scales can be obtained from the Fourier-transform of real-time DFT/MD trajectories or from equation of motion techniques,²¹ which give for the density of modes $\rho_R(\omega)$,

$$\rho_R(\omega) = \int_0^\infty \langle R(0) \cdot R(t) \rangle \cos(\omega t) e^{-\epsilon t} dt, \quad (8)$$

where $\langle R(0) \cdot R(t) \rangle$ is the autocorrelation function of the coordinate of interest R and ϵ is a broadening parameter added for convenience.

D. Thermal fluctuations at the nanoscale

Part of the driving force behind DSD is due to the large thermal fluctuations in nano-scale clusters, which is briefly explored here. As noted in the Introduction, thermal properties of nano-structures with relatively small N differ substantially from those in macroscopic condensed matter due to finite-size effects enhanced by their poor thermal coupling to the support. As in bulk systems, their total thermal energies at a given substrate temperature T are not sharply defined, but exhibit substantial energy fluctuations¹⁷ of order $kT\sqrt{N}$. Moreover, these variations lead to substantial long-time fluctuations in the local temperature (or energy per particle) of order T/\sqrt{N} . This latter effect is not immediately obvious since the global temperature T is a constant throughout the system, as fixed by the substrate. To understand these results, we recount the classical arguments of statistical thermodynamics. We consider a nano-cluster with N atoms weakly bound to a support at fixed temperature T , which serves as a heat-bath. For simplicity of argument the cluster volume V , charge Q , and composition can be regarded as fixed, but these constraints are not essential and will be relaxed below. Due to contact with the support, which is in continuous thermal and vibrational motion, energy will fluctuate between the cluster and the support, with a probability distribution

$$P(E, T) \approx \Omega(E) e^{-\beta E} = e^{-\beta \mathcal{F}(E, T)}, \quad (9)$$

where $\mathcal{F}(E, T) = E - TS(E)$ and $k \ln \Omega(E) = S(E)$ is the net cluster entropy due to distinguishable configurations $\Omega(E)$ of the nano-cluster at energy E . True thermal equi-

librium corresponds to the maximum probability or, equivalently, $\min \mathcal{F}(\bar{E}, T) = F(T)$, which in bulk thermal equilibrium would correspond to the Helmholtz free energy. The mean total cluster energy \bar{E} is then fixed by the relation $\partial S(E)/\partial E|_{\bar{E}} = 1/T$, and hence both the nano-cluster and the support will have the same average temperature T . The cluster entropy $S(E)$ is additive in terms of the independent $6N$ degrees of freedom in the cluster dynamics. In addition to the $(3N - 3)$ internal vibrational modes (including both potential and kinetic degrees of freedom), the SRR dynamics include four additional degrees of freedom from the 2-d librational modes of the CM parallel to the support, and additional modes binding the cluster to it. The distribution $P(E, T)$ is sharply peaked for large N and approximately Gaussian near the peak at \bar{E} . However, due to fluctuations the most probable value may differ from the thermal equilibrium value.¹⁸ The mean square energy fluctuations σ_E^2 are obtained from the 2nd derivative of the entropy $\sigma_E^2 = k/[\partial^2 S(E)/\partial E^2]$. The quantity σ_E^2 is clearly $O(N)$ since both the total energy E and entropy $S(E)$ of the cluster are extensive. At high temperatures, where equipartition is valid, $\bar{E} = 3NkT$ and $S(E) \approx 3Nk \ln E$. Thus the energy fluctuations are given by $\sigma_E \propto kT\sqrt{3N}$ and similarly since $T = \bar{E}/3Nk$, fluctuations in the internal temperature of the cluster are $\sigma_T = T/\sqrt{3N}$. The effect is rather like that of a fluctuating thermostat for which any nonlinear effects on temperature (e.g., reaction rates) do not cancel. This effect shows up in DFT/MD calculations of the total energy per particle, and we have found that the effect persists in substantial long-time fluctuations of ps time-scales. Consequently, one may expect substantial DSD effects on reaction rates. For example, for $N = 20$ at 600 K, \bar{E} is distributed within a few tenths of an eV of the mean $\bar{E} = 3NkT \approx 3$ eV, and $\sigma_T \approx 75K$. In contrast, the thermal fluctuations of the semi-infinite substrate itself are negligible. This statistical argument suggests why finite temperature DFT/MD approaches may be more efficient than full canonical ensemble sampling for calculating the physical properties of nanoclusters, since they naturally probe the range of accessible phase space within a few σ_E of \bar{E} over a time-scale comparable to the periods of vibrational and librational motion.

The above arguments can be generalized for other conserved physical quantities, for example total volume $V_{tot} = V + V_S$, net electronic charge $Q_{tot} = Q + Q_S$, chemical composition, etc., where the subscript S refers to the support. To this end one must generalize the calculations of accessible states in terms of $S(E, V, Q, N_i)$ with varying V , Q , etc. These additional physical quantities are stabilized by those from the support bath, so that $F \rightarrow F - pV + \mu Q/e + \sum_i \mu_i N_i$ where p is the pressure, μ the chemical potential, Q/e is the number of electrons in the cluster, and N_i is the number of atoms of species i . Since quantities like V and Q are extensive, one also expects their fluctuations to be of order $N^{1/2}$. The charge (and hence chemical potential) fluctuations, are important to explain the variation of the Fermi energy with temperature in the XAS studies.⁶ Due to the strength of Coulomb forces and the importance of oxidation states in many catalytic reactions, these charge fluctuations may play a key role in controlling nano-scale properties and chemical reaction rates.

III. EFFECTS OF DSD ON NANOSCALE REACTIONS

A. Effects of fluctuations in nanoscale reaction rates

Formally, calculations of catalytic properties such as reaction rates depend on free energies from equilibrated statistical ensembles that contain all accessible regions of phase space. Some effects of disorder^{22,23} and the presence of a variety of possible transition paths^{24,25} have been addressed in the past. Due to its simplicity, however, transition state theory (TST) is still the most widely used approach for rate calculations in molecular and nanoscale systems.²⁶ This approach is usually based on time-independent nanoparticle potential energy surfaces and the assumption of quasi-equilibrium between reactants and transition state. In contrast, our SRR model based on finite-temperature DFT/MD calculations avoids many of these difficulties. We stress that *ab initio* DFT/MD is crucial for many properties, as classical MD simulations with model potentials do not adequately capture charge fluctuations, bond-breaking, diffusion, and other non-equilibrium effects.²⁷ Moreover DFT/MD is a good approach for non-equilibrium structural and physical properties at high temperatures, since it builds in anharmonic and structural disorder.

Statistical thermodynamic arguments similar to those in Sec. II D can be applied to nano-scale reaction rates. Our analysis below suggests that it may be important to treat the behavior of reactant molecules on the dynamically fluctuating surface of a nano-cluster, e.g., with our SRR model, rather than on selected static structures. Thus, the slow fluctuating modes of both the cluster and the reactant molecules can now couple, resulting in an statistical ensemble of reaction barriers and reaction rates.

The SRR catalysis model thus consists of a system of reactant molecules in contact with a fluctuating cluster that can exchange energy to and from it. Our treatment below focuses on the rate limiting step of crossing the transition barrier. More detailed approximations should take into account the diffusion rates of the molecules on the surface of the nano-clusters to the reaction site. Given that diffusion processes are dominated by low frequency modes, such rates are likely influenced by the slow nature of the DSD. Using arguments analogous to those of Sec. II D, the probability distribution $P(\epsilon)$ of reactant energies ϵ is given by a statistical ensemble with a fluctuating cluster energy distribution E relative to the mean \bar{E} : $\Omega(E - \epsilon) \propto \exp[S(E) - \tilde{\beta}\epsilon]$ where $\tilde{\beta} = \partial S(E)/\partial E = 1/k\tilde{T}$ is the fluctuating inverse local cluster temperature at energy E . Thus we obtain

$$P(\epsilon) \approx \langle \Omega_R(\epsilon) e^{-\tilde{\beta}\epsilon} \rangle = \langle e^{-\tilde{\beta}f(\epsilon;\tilde{T})} \rangle, \quad (10)$$

where $\Omega_R(\epsilon)$ is the configurational entropy of the reactant molecules on the cluster, and the average is carried out over the distribution of cluster energies E and hence values of $\tilde{\beta}$. This result shows why the average over terms with $\tilde{\beta}$ is not the same as that with fixed β when temperature fluctuations are large.

Consequently, calculations of reaction rates κ for the transition $[A] + [B] \rightarrow [AB^*] \rightarrow [P]$ require a generalization

of transition state theory to the case with fluctuating barriers,

$$\kappa = \frac{kT}{h} \left\langle \frac{\tilde{Z}_{AB}^*}{\tilde{Z}_A \tilde{Z}_B} e^{-\tilde{\beta}\epsilon_b} \right\rangle. \quad (11)$$

Here h is Planck's constant, and the averages in the partition functions are carried out over all nano-cluster configurations, Z_{AB}^* is the partition function of the activated complex, and Z_A and Z_B the partition functions of the reactants A and B , and again the average is carried out over the range of local temperatures $\tilde{\beta}$. This result is analogous to the usual Arrhenius law, but with a dynamically averaged "attempt frequency" prefactor and fluctuating reaction barriers $\langle e^{-\tilde{\beta}\epsilon_b} \rangle$. Both of these factors are affected by DSD. It is easy to see, for example, using a first order cumulant expansion, why the latter average is always greater than the reactivity at the mean barrier $\langle \epsilon_b \rangle$

$$\langle e^{\tilde{\beta}\epsilon_b} \rangle = e^{-\tilde{\beta}\langle \epsilon_b \rangle} e^{(1/2)\tilde{\beta}^2 \sigma_{\epsilon_b}^2} \geq e^{-\tilde{\beta}\langle \epsilon_b \rangle}. \quad (12)$$

The average leads to a reduced, temperature dependent "effective barrier" $\epsilon'_b = \epsilon_b - (1/2)\tilde{\beta}\sigma_{\epsilon_b}^2$, which is comparable to the lowest barriers typically encountered during reactions. Note, however, that the cumulant estimate assumes small fluctuations in ϵ_b , more generally the inequality is always valid and the lowest barriers dominate.

Approximate calculations of the molecular partition functions in these fluctuating TST models can be carried out in terms of the *local free energies* of the molecules bonded to the fluctuating cluster or at the transition state using a generalization of the coupled-oscillator model discussed above. One expects that the low frequency modes of the reacting molecule will be strongly coupled to the cluster and depend both on the instantaneous orientation and local geometry of the molecule on the cluster surface at a given time. This coupling is expected to be transient, and it is plausible that cluster fluctuations will assist a molecule in probing a wider range of degrees of freedom than on a static support. Within this model, the local free energy of an adsorbed molecule with position \vec{r} is given by

$$f(\vec{T}) = \epsilon_0(\vec{r}) + k\tilde{T} \int d\omega \rho_R(\omega) \ln[2 \sinh(\tilde{\beta}\hbar\omega/2)], \quad (13)$$

where $\rho_R(\omega)$ is the projected local density of vibrational states at a given reactant molecule at position \vec{r} on the surface of the cluster and \vec{T} is the effective temperature of the cluster. As with the total free energy of the cluster, the local free energy of the molecule $f(\vec{T})$ contains terms coupling to the fast vibrational density of states of the cluster, and to the relatively slow librational motion of the CM and other contributions to DSD. Since reactant molecular vibration frequencies are often large compared to thermal motion ($\hbar\omega \gg kT$), their vibrational states are typically frozen in their ground state, and the classical high temperature limit is inappropriate. On the other hand, relatively low energy bending and rotational modes may be thermally active and hence contribute strongly. As with DSD, one expects that the MSR σ^2 of the reactant molecule will contain contributions from the low frequency librational modes, even for weak couplings as contributions to σ^2 are proportional to $1/\omega^2$ (cf. Fig. 5 of Ref. 19). Thus it is possible that these low frequency fluctuations can significantly increase the entropy fluctuations and hence the catalytic

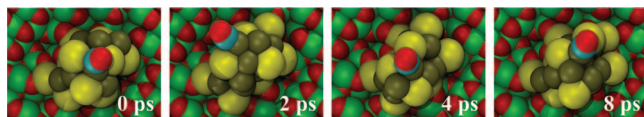


FIG. 5. Structural snapshots of the dynamics of CO on $\text{Pt}_{10}\text{Sn}_{10}$ on $\gamma\text{-Al}_2\text{O}_3$ at 598 K. Here the sphere colors represent: red, oxygen; blue, carbon; green, aluminium; yellow, tin; brown, platinum. These snapshots show that the CO molecule remains tethered to a Pt atom through its C-end for most of the simulation time, despite the high mobility on the surface.

activity of reactants, though quantitative calculations are needed to assess the net effect.

B. DSD and adsorbate dynamics

As an illustration of the concepts discussed above, we present calculations and sample reaction paths for prototypical molecules adsorbed on nano-clusters. In order to address the effects of DSD on their catalytic activity we first address the “simpler” problem of adsorbate dynamics on the surface of the particles. This approach serves two main purposes: First, it probes the coupling between the adsorbate dynamics and the dynamical disorder, which is key to understanding reactivity, in particular in the pre-transition state regime. Second, given that vibrational spectra of adsorbates are readily available, it provides a good benchmark for the DFT/MD simulations showing whether they are capable of reproducing the dynamics of adsorbed molecules. Thus, we have carried out DFT/MD simulations similar to those described in Secs. II B and II C, but with the addition of an adsorbate molecule (CO) on the surface of the nanoparticle. Fig. 5 shows a series of snapshots illustrating the high mobility of the molecule over the surface.

Qualitatively, while the CO molecule position is strongly coupled to the DSD of the nanoparticle, its internal structure is not expected to depend strongly on disorder. The MD simulations support this statement: First, the CO molecule is tethered to a Pt atom through its carbon-end for most of the simulation, so its position is modulated by the slow Pt motion. Nevertheless, brief incursions into bridging sites are also observed. These noticeably affect the internal structure of the adsorbate by elongating the CO bond. Second, the low frequency dynamics associated with DSD are likely to couple better with the low frequency C–Pt bonds, rather than with the high frequency adsorbate covalent bonds.

To investigate this coupling between the adsorbate dynamics and the nanoparticle DSD more quantitatively, we have filtered out the slow, stochastic component from the intra-adsorbate (R_{CO}) and adsorbate-particle (R_{CPt}) dynamics, similar to that in Fig. 4. The fast transition between Pt anchoring points described above can be clearly seen in a typical trajectory (Fig. 6). Here the region between $\sim 2\text{--}4$ ps shows the brief incursions into bridging sites. These transient states have a clear effect on the internal structure of the adsorbate as seen in Fig. 7, which shows the decomposition of the R_{CO} dynamics into vibrational and disorder components. The transient mean bond distance (represented by the red “Disorder” curve) is increased in the bridging site, while the amplitude of

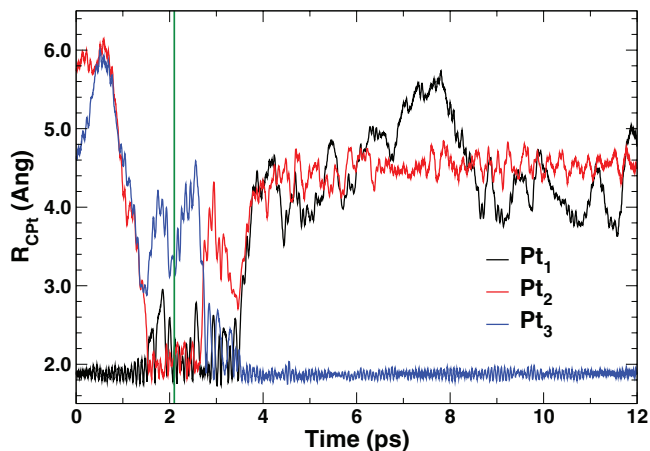


FIG. 6. Dynamics of the three shortest R_{CPt} bonds in a typical trajectory for CO adsorbed on $\text{Pt}_{10}\text{Sn}_{10}$ on $\gamma\text{-Al}_2\text{O}_3$ at 598 K. The vertical green line indicates the end of the thermalization stage. The region between $\sim 2\text{--}4$ ps shows fast transitions between Pt anchoring points, with brief incursions into bridging sites. These states have a clear effect on the R_{CO} distance (Fig. 7).

the vibrational component (blue “Vibrational” curve) is enhanced due to the weakened bond.

The projected densities of states $\rho_R(\omega)$ for each component of these trajectories can be calculated using Eq. (8), and are shown in Fig. 8 (top). The most prominent features correspond to the CO stretch for both on-top (between 60 and 64 THz, or 2001 to 2135 cm^{-1}) and on-bridge (small peaks between 54 and 58 THz, or 1800 to 1935 cm^{-1}). These frequency ranges are in good agreement with the experimental values.^{28–31} Also noticeable is a small feature between 12 and 16 THz (400 and 535 cm^{-1}) associated with the molecule-particle interaction, as discussed below in further detail. As expected, the negligible weight of the disorder confirms that the intramolecular dynamics of CO are largely independent of DSD.

The disorder has a much larger role in the molecule-nanoparticle dynamics, as seen in Fig. 8 (middle), where the R_{CPt} modes below 5 THz (170 cm^{-1}) are highly coupled to the DSD. The vibrational component shows a prominent feature between 13 and 15 THz (430 and 500 cm^{-1}), in

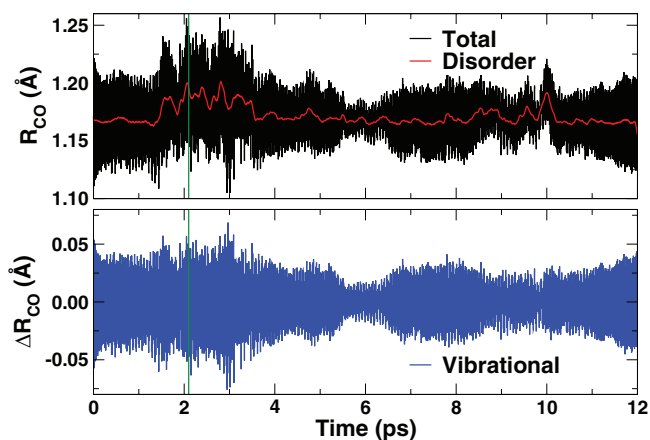


FIG. 7. Decomposition of the R_{CO} dynamics (black) into vibrational (blue) and DSD (red) components for CO adsorbed on $\text{Pt}_{10}\text{Sn}_{10}$ on $\gamma\text{-Al}_2\text{O}_3$ at 598 K. The vertical green line indicates the end of the thermalization stage.

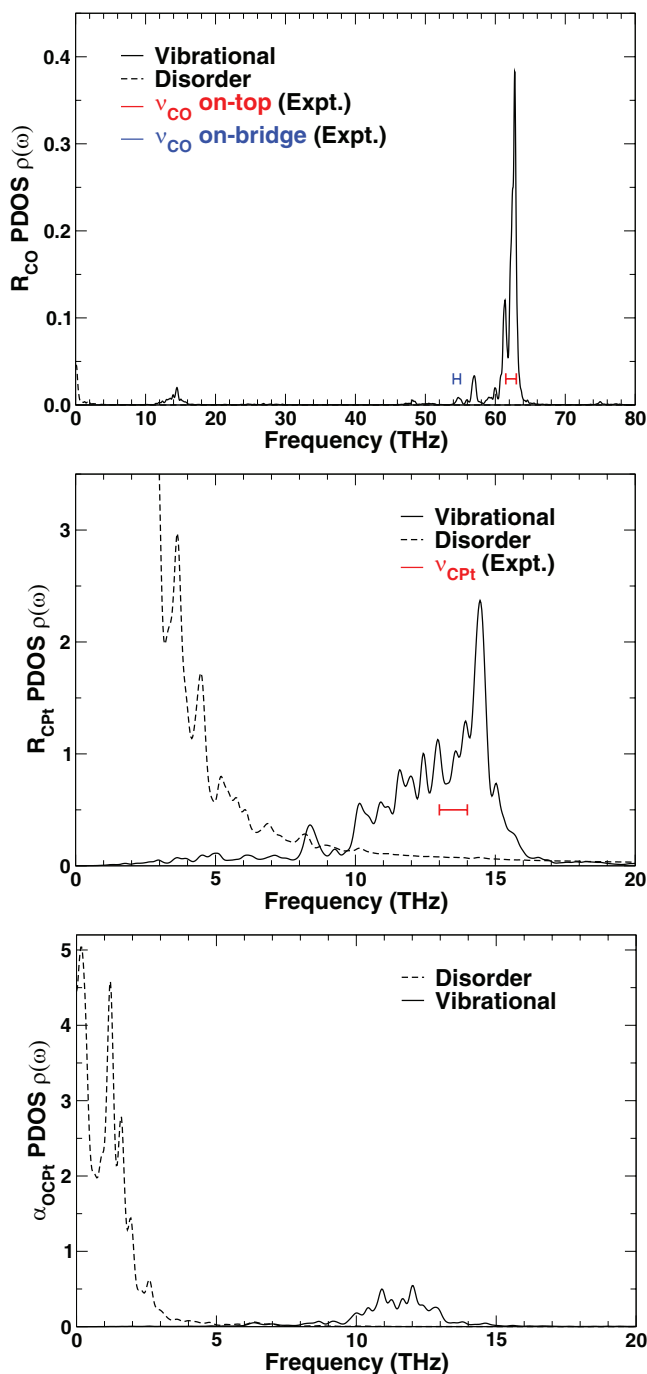


FIG. 8. Average projected density of states for the vibrational and DSD components of the R_{CO} (top), R_{CPt} (middle), and $PtCO$ (α_{OCPt} , bottom) trajectories in $Pt_{10}Sn_{10}$ on $\gamma-Al_2O_3$ at 598 K. The experimental CO stretch frequency for on-top adsorption sites ranges from 61.5 to 63 THz (2050 to 2100 cm^{-1}), while for on-bridge sites it ranges from 54 to 55 THz (1800 to 1835 cm^{-1}). For the C–Pt stretch, the frequency ranges from 13 to 14 THz (434 to 467 cm^{-1}).

reasonable agreement with the experimental range of 13–14 THz (434 to 467 cm^{-1}) for the C–Pt stretch mode.³² In addition, the R_{CPt} dynamics show a broad feature between 10 and 13 THz (334 to 434 cm^{-1}) which results from strong coupling to the $PtCO$ bending, as seen in Fig. 8 (bottom). The large component of disorder in the R_{CPt} and $PtCO$ coordinates highlights the importance of nanoparticle fluctuations on the pre-dissociation regime where the reacting molecule

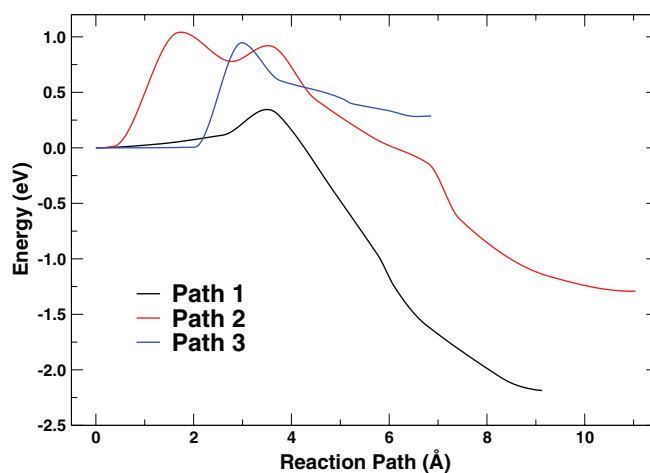


FIG. 9. Typical NEB reaction paths for the dissociation of O_2 on fully relaxed $Pt_{10}Sn_{10}$ supported on $\gamma-Al_2O_3$. Path energies have been shifted to match at the reactant state. The reaction path coordinate corresponds to the integrated displacement of all atoms in the system.

both explores a variety of surface sites, and the physical properties of the sites themselves vary dynamically. Moreover, it points to an enhanced role of disorder during the reaction regime, where the breaking bonds become weaker. In this regime we expect the frequencies associated with the reaction path to be lowered into the disorder-dominant region and thus become more coupled with DSD.

C. Effects of DSD on reaction barriers

As discussed in Sec. III A, the DSD creates an effective activation barrier $\epsilon'_b \leq \epsilon_b$ due to barrier fluctuations. To study these fluctuations, we performed nudged elastic band (NEB) calculations of the dissociation of O_2 on $Pt_{10}Sn_{10}$ supported on $\gamma-Al_2O_3$. Fig. 9 shows results for three sample reaction paths, generated for nanoparticle conformations with different DSD, sampled from DFT/MD trajectories. In principle, the different nanoparticle conformations should be sampled from MD trajectories including the adsorbate. In practice, however, the effect of the latter is local and largely does not affect the overall dynamics of the nanoparticle. Nevertheless, given the poor sampling implied by the use of just three paths, these simulations should be regarded as proof-of-principle. Fig. 10 shows the structures of the initial, transition, and final states for these reaction paths. These paths represent rather different behaviors, including exothermic and endothermic thermodynamics, and the presence of a high energy intermediate in path 2. We find that reactions paths starting in perpendicularly absorbed molecules go through a very stable intermediate state where the O_2 molecule is oriented parallel to the surface. Thus, we only show those portions of the paths. Despite their similar orientations, the initial states correspond to adsorption on sites with different local environments. For instance, while path 1 starts with absorption on top of a single Pt atoms, paths 2 and 3 start with absorption over a Pt–Sn bond. Although the activation barriers occur close to the initial state, and thus the initial and transition states (TS) have similar structural characteristics, the activation energy of

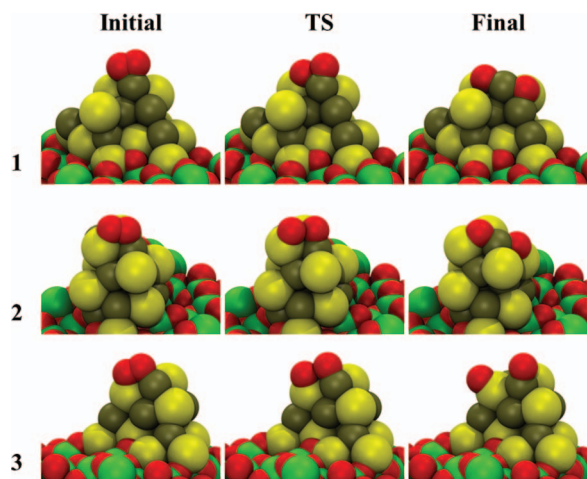


FIG. 10. Initial, transition and final states for the NEB reaction paths (1-3, as in Fig. 9) for the dissociation of O_2 on fully relaxed $Pt_{10}Sn_{10}$ supported on γ - Al_2O_3 . The sphere colors represent: red, oxygen; green, aluminium; yellow, tin; brown, platinum.

path 1 is significantly lower to those of the other paths. This is due to the relative stabilization of the TS in 1 through the incipient formation of a strong O–Sn bond. The difference in relative final state energies are also related to the strength of the bonds O–Sn bonds formed: path 3 has the O atoms forming only single bonds to Pt and Sn atoms, and thus results in a less stable structure. Paths 1 and 2 have final states where the O atoms form multiple anchors to the nanoparticle that make them very stable. From these results we can roughly estimate the mean barrier ($\epsilon_b \simeq 0.8$ eV), and the barrier fluctuations ($\sigma_{\epsilon_b} \simeq 0.5$ eV). In addition, we can estimate the nanoparticle distortions induced during the dissociation process by analyzing the atomic displacements along the reaction path. For the paths shown in Fig. 9, the metal atoms directly bound to the O_2 molecule experience displacements of the order of 0.2 Å along the reaction path. Such nanoparticle distortions are of similar magnitude to those observed due to DSD (0.2–0.4 Å). The remainder of the nanoparticle also participates in the reaction, but with smaller displacements of order 0.1 Å.

The effects of DSD on the reaction barriers are twofold: First, direct effects change the chemical nature of the reactants, transition states, and products. These direct effects are usually visible as large energy changes, such as the shift from endothermic to exothermic behavior in paths 3 and 2, respectively, and are driven by major rearrangements of the structure of the nanoparticle and its interaction with the adsorbate. Second, smaller fluctuations in structure that do not change the chemical nature of the different states yet still induce changes in the activation barrier. To quantify these indirect effects we have also computed reaction barriers where all atoms, except those in the dissociating O_2 molecule, are fixed at the transition state structure of the paths in Fig. 9. These rigid nanoparticle paths are shown in Fig. 11. Overall, these paths are smoother than the fully relaxed ones. For example, the nanoparticle fluctuations induce a variety of minima and shoulders in the reaction path. Given that both the nanoparticle and surface are fixed at the structure of the fully relaxed transition state, by definition the rigid reaction paths map to

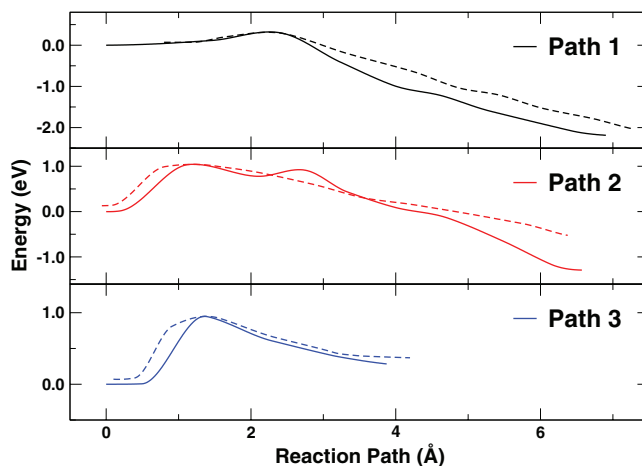


FIG. 11. Comparison of the fully relaxed NEB reaction paths for the dissociation of O_2 on $Pt_{10}Sn_{10}$ supported on γ - Al_2O_3 (full lines) with the reaction paths obtained by fixing the surface and nanoparticle structure at the transition state conformation (dashed lines). The energies for the fully relaxed paths have been shifted to match at the reactant state. The reaction path coordinate corresponds to the integrated displacement of all relaxed atoms in the system.

higher energies in the potential energy surface, resulting in smaller barriers. This does not preclude the fact that, on average, the dynamic disorder tends to reduce the reaction barriers. The difference is only 0.1–0.2 eV, but clearly the effect on the exponential character of reaction rates is nevertheless substantial. This result demonstrates our premise that DSD in nano-structures can significantly affect reaction rates.

IV. CONCLUSIONS

We have investigated the effects of dynamic structural disorder on the properties of supported metal nanoparticles, from both their morphological and reactivity perspectives. Our primary focus is on aspects of DSD that have not been adequately described previously. Our results suggest that a real-time approach that accounts for their fluctuating bonding and electronic structure provides a powerful method to better understand their catalytic activity. In particular, we have found that the DSD in nanoclusters is an important concept for understanding structural disorder. This can be probed by techniques like EXAFS, where disorder has typically been accounted for in terms of globally averaged properties. In addition, our real time approach can be especially important in interpreting time-resolved x-ray spectroscopy experiments, such as those performed using x-ray free electron laser sources. Moreover, the possible effects of DSD on reaction paths and reaction rates in supported nano-scale catalysts has not, to our knowledge, been carefully elucidated previously. DSD leads to a larger statistical ensemble of configurations than that from thermal vibrations plus static disorder on solid surfaces and overlayers. The SRR concept makes it possible to simulate the statistical ensemble of possible reaction sites efficiently, compared to the effort needed for enumerating structures and Boltzmann factors. It can reveal both the surface structure and dynamics, which can be more important than the global average morphology typically measured in

experiment. Since experimental probes of nano-scale systems measure their global average properties, it is important in the analysis to differentiate between surface and internal structure. Our results highlight the strong coupling between the surface disorder and the adsorbate dynamics which is likely to have significant consequences in reactivity. In addition, the local electronic structure of the binding sites is highly heterogeneous. For example, the oxidation state of a Pt atom varies significantly depending on its local environment. Thus, the DSD in these systems effectively induces additional active sites for reaction pathways, which likely account for the increased reaction rates in nano-scale systems. Our results emphasize the importance of large fluctuations driven by the stochastic motion of the center of mass of the nanoparticles and their transient bonding to the support. These fluctuations affect the internal energy and temperature distribution as well as the structure of the nanoparticles, thus having a measurable effect on both the properties observed by experimental. They also affect both the prefactors and distribution of energy barriers, thus tending to increase the observed reaction rates. Consequently, we believe the SRR model of dynamic structural disorder constitutes a timely integration of concepts that provides a compelling understanding of disorder phenomena in nano-catalysts with potentially wide ranging implications.

ACKNOWLEDGMENTS

The authors wish to thank S. R. Bare, J. J. Kas, S. D. Kelly, M. Tromp, and especially A. Frenkel for advice and useful references. This work was supported by DOE Grant No. DE-FG02-03ER15476 with substantial computer support from DOE-NERSC.

¹S. J. L. Billinge and I. Levin, *Science* **316**, 561 (2007).

²S. Link and M. A. El-Sayed, *Annu. Rev. Phys. Chem.* **54**, 331 (2003).

³V. Johánek, M. Laurin, A. W. Grant, B. Kasemo, C. R. Henry, and J. Libuda, *Science* **304**, 1639 (2004).

⁴F. D. Vila, J. J. Rehr, S. D. Kelly, and S. R. Bare, *J. Phys. Chem. C* **117**, 12446 (2013).

⁵J. H. Kang, L. D. Menard, R. G. Nuzzo, and A. I. Frenkel, *J. Am. Chem. Soc.* **128**, 12068 (2006).

⁶F. Vila, J. J. Rehr, J. Kas, R. G. Nuzzo, and A. I. Frenkel, *Phys. Rev. B* **78**, 121404(R) (2008).

⁷D. F. Yancey, S. T. Chill, L. Zhang, A. I. Frenkel, G. Henkelman, and R. M. Crooks, *Chem. Sci.* **4**, 2912 (2013).

⁸H. Topsøe, *J. Catal.* **216**, 155 (2003).

⁹M. Boero, M. Parrinello, and K. Terakura, *J. Am. Chem. Soc.* **120**, 2746 (1998).

¹⁰V. L. Schramm, *J. Biol. Chem.* **282**, 28297 (2007).

¹¹W. Min, B. P. English, G. Luo, B. J. Cherayil, S. C. Kou, and X. S. Xie, *Acc. Chem. Res.* **38**, 923 (2005).

¹²J. H. Ryu, D. H. Seo, D. H. Kim, and H. M. Lee, *Phys. Chem. Chem. Phys.* **11**, 503 (2009).

¹³P. Jensen, A. Clément, and L. J. Lewis, *Comput. Mater. Sci.* **30**, 137 (2004).

¹⁴S.-P. Huang, D. S. Mainardi, and P. B. Balbuena, *Surf. Sci.* **545**, 163 (2003).

¹⁵P. A. Thiel, M. Shen, D.-J. Liu, and J. W. Evans, *J. Phys. Chem. C* **113**, 5047 (2009).

¹⁶T. W. Hansen, A. T. DeLaRiva, S. R. Challa, and A. K. Datye, *Acc. Chem. Res.* **46**, 1720 (2013).

¹⁷L. D. Landau and E. M. Lifshitz, *Course of Theoretical Physics, Vol. 5, Statistical Physics*, 3rd ed., Part I (Butterworth-Heinemann, Oxford, 1980), pp. 340–341.

¹⁸L. Rubinovich and M. Polak, *Nano Lett.* **13**, 2247 (2013).

¹⁹F. D. Vila, J. J. Rehr, H. H. Rossner, and H. J. Krappe, *Phys. Rev. B* **76**, 014301 (2007).

²⁰G. Kresse and J. Furthmüller, *Phys. Rev. B* **54**, 11169 (1996).

²¹F. D. Vila, V. E. Lindahl, and J. J. Rehr, *Phys. Rev. B* **85**, 024303 (2012).

²²R. Zwanzig, *Acc. Chem. Res.* **23**, 148 (1990).

²³R. Zwanzig, *J. Chem. Phys.* **97**, 3587 (1992).

²⁴P. G. Bolhuis, D. Chandler, C. Dellago, and P. L. Geissler, *Annu. Rev. Phys. Chem.* **53**, 291 (2002).

²⁵C. Dellago, P. G. Bolhuis, and D. Chandler, *J. Chem. Phys.* **108**, 9236 (1998).

²⁶D. G. Truhlar, B. C. Garrett, and S. J. Klippenstein, *J. Phys. Chem.* **100**, 12771 (1996).

²⁷H. Jónsson, *Annu. Rev. Phys. Chem.* **51**, 623 (2000).

²⁸K. Kung, P. Chen, F. Wei, Y. Shen, and G. Somorjai, *Surf. Sci.* **463**, L627 (2000).

²⁹K. McCrea, J. S. Parker, P. Chen, and G. Somorjai, *Surf. Sci.* **494**, 238 (2001).

³⁰K. R. McCrea, J. S. Parker, and G. A. Somorjai, *J. Phys. Chem. B* **106**, 10854 (2002).

³¹G. Hu, H. Gao, and C. T. Williams, *J. Phys. Chem. C* **116**, 6247 (2012).

³²M. T. Paffett, S. C. Gebhard, R. G. Windham, and B. E. Koel, *J. Phys. Chem.* **94**, 6831 (1990).